The ideal flip-through impact: experimental and numerical investigation

H. Bredmose · A. Hunt-Raby · R. Jayaratne · G. N. Bullock

Abstract Results from a physical experiment and a numerical computation are compared for a flip-through type wave impact on a vertical face, typical of a seawall or breakwater. The physical wave was generated by application of the focused-wave group technique to the amplitudes of a JONSWAP spectrum, with the focus location adjusted to produce a near-breaking wave impact with no discernible air entrainment or entrapment. Details of the resultant impact are presented in the form of high-speed video, pressure transducer and wave gauge records. Numerical reproduction of the wave transformation and impact is achieved by application of a linear wave-analysis model and a fully nonlinear potential-flow solver. Although more advanced models exist, use of the latter model type is interesting as (1) it was applied by Cooker and Peregrine (Proceedings of the 22nd International Conference on Coastal Engineering, 164–176, 1990) in their original numerical discovery of the flip-through impact and (2) the assumptions behind the potential-flow model remain reasonably valid, until the flip-through jet begins to break into droplets. In the present study, the potential-flow model has been extended with the Schwarz–Christoffel conformal mapping, to allow a piece-wise linearly shaped mound geometry. Further, an ad-hoc wave-generation technique has been added, to facilitate an adequate numerical reproduction of long second-order waves in the flume. Free-surface elevations from the potential-flow computations show good agreement with wave gauge data for the wave that produces the flip-through impact. Experimental video frames with the corresponding numerical free-surface profiles overlaid show an excellent match for the flow contraction prior to impact. The deviations between the experiment and numerical solution that occur at the stage of jet formation are discussed and a computation of a slightly weaker impact illustrate the strong sensitivity of impact pressures to the shape of the impacting wave. Ways of improving the numerical description by use of more advanced models are outlined.

Keywords Coastal engineering · Focused wave groups · Impact pressures · Potential flow · Violent wave impacts

H. Bredmose (✉)
DTU Mechanical Engineering, Niels Koppels Allé, Building 403, 2800 Kgs. Lyngby, Denmark
e-mail: hbr@mek.dtu.dk

A. Hunt-Raby · G. N. Bullock
School of Marine Science and Engineering, University of Plymouth, Drake Circus, Plymouth PL4 8AA, UK

R. Jayaratne
School of Computing, Information Technology and Engineering, University of East London, 4-6 University Way, London E16 2RD, UK

1 Introduction

The loads associated with violent breaking-wave impacts must be taken into account during the design of many types of coastal and marine structures. In this paper we consider the case of a vertical wall, where the flip-through impact has received increased scientific attention since the numerical discovery of Cooker and Peregrine [1].

When the waves are too low to break, the water tends to rise up and down the face of a vertical wall in a process sometimes known as 'sloshing'. Most of the wave energy is reflected and the structure is subject to relatively benign 'pulsating' loads. A violent impact occurs when the front of the wave steepens and becomes more or less vertical just before it reaches the wall. Both physical and numerical models indicate that the highest impact pressures are associated with situations in which the crest of the wave has begun to turn over so that a small pocket of air is trapped between the water and the structure, see for example [2–5].

Flip-through impacts occur within a narrow range of wave conditions on the border between sloshing and the violent impacts associated with an overturning wave crest. The term 'flip-through' was coined by Cooker and Peregrine [1] on the basis of their findings from fully nonlinear potential-flow computations. These indicated that the approach of a vertical wave front does not always lead to a direct impact between solid water and the wall. This is because, in some circumstances, the volume flux from below the crest can cause such a rapid rise in the water level against the wall that a vertical jet is formed which flips up through the gap in front of the approaching wave. Although the jet prevents the wave front from coming into direct contact with the wall, the computations demonstrated that the resultant smooth flow could still generate very large localised pressures on the wall.

Flip-through impacts are associated with strong accelerations at the wall where the vertical jet emerges. Cooker and Peregrine [6] reported vertical accelerations exceeding 10.000 g. Through the Euler equation $\mathrm{D}\mathbf{u}/\mathrm{D}t = -\nabla p/\rho - \mathbf{g}$ (where $\mathbf{g} = (0, 0, g)$), this is associated with a strong pressure gradient which in turn is linked to the high pressures at the wall. In such circumstances, the contribution of gravitational acceleration to the pressure gradient is negligible. This means that the orientation of a flip-through impact relative to the direction of gravity is unimportant for the local pressure field at impact. Further results and discussion of flip-through impacts in the context of potential-flow computations have been given by Cooker and Peregrine [7] and Peregrine [8].

The idealised 2D nature and strong spatial localisation of the impact zone make the physical investigation of flip-through impacts difficult. At its simplest, this means that the point of maximum pressure may well occur at a point where no transducer has been placed. History effects and transverse non-uniformities in the shape of waves can introduce more complex phenomena leading to a high degree of variability between measurements obtained both at a particular point during the impacts of a number of nominally identical waves and from points at the same elevation across the channel during a single impact as reported by [4].

A limited number of experimental studies of flip-through impacts exist in the literature. Whilst the results of Cooker and Peregrine [1] were based on a steep wave in shallow water, Chan and Melville [9] had already reported experimental observations of a similar type of impact in deep water. The impacts occurred at a surface-piercing vertical plate that stopped short of the sea bed. Hattori et al. [3] conducted an experimental study of breaking-wave impacts on a vertical wall including a flip-through impact. The study was based on regular waves. High-speed video at 200 frames per second and pressure time histories were presented. Hull and Müller [10] conducted experiments on breaking-wave impacts on a vertical wall. During each impact three flash guns were sequentially activated in front of an open camera, to freeze the motion at three time instants onto a single image frame. Among the impacts investigated, the pre-stage of a flip-through impact was presented with a characteristic vertical front. The pressure time histories showed a distinct pressure peak with no trace of aeration effects. Lugni et al. [11] conducted an experimental study of flip-through impacts in a sloshing tank. High-speed video imaging was combined with a specialised PIV method to allow detailed analysis of the flow evolution and internal flow kinematics. Accelerations of up to 1500 g were measured in the vertical jet. Three modes of flip-through impacts were defined, the first being characterised by no entrapment of air, while the second and third mode were associated with entrapment of a single air pocket and a multitude of air bubbles, respectively. We do not widen the definition of a flip-through impact to cover all these cases but follow [1,8] and adopt the classical position that no air is trapped in a flip-through impact.

Numerical flip-through impacts as identified by Cooker and Peregrine [1] represent an idealised incompressible description of violent wave impacts. Modelling in terms of potential-flow theory is only possible because there is no direct impact of water on the wall and no air is trapped. In practice, even if a particular wave does not trap any additional air, the water is likely to contain air that has been entrained during earlier events and this will increase the compressibility of the water phase. Numerical computations which include the effect of trapped and entrained air have been presented by Bredmose et al. [5] who also modelled a flip-through impact. As already indicated, this study confirmed the observation that the strongest impact pressures occur when a small air pocket is trapped at the wall. The results also illustrated that while in potential-flow computations there is a clear demarcation between flip-through and overturning impacts, this boundary is less well defined for physical impacts. Reasons for this include mixing of water and air, transverse modulations of the wave motion and small-scale imperfections in the shape of the free surface due to turbulence. The free surface may be further disrupted by a non-uniform flow of air in the gap between the wave front and the wall.

Besides the work of Cooker, Peregrine and their collaborators, only a few numerical studies of flip-through impacts have been published. Colicchio et al. [12] applied a level-set method and an SPH (Smoothed Particle Hydrodynamics) method to model an impact which trapped a small pocket of air. The impact was achieved in the same tank as that of Lugni et al. [11]. Although the global numerical free-surface profiles inside the tank and the initial rise of the pressure peak were in good agreement with the physical experiment, the detailed position of the air pocket and its oscillatory dynamic pressure after the main impact peak was not reproduced by the numerical models. Khayyer and Gotoh [13] developed several modified forms of the MPS (Moving Particle Semi-implicit) method which they compared with the results of Hattori et al. [3] for a flip-through impact. Whilst they demonstrated that the best of their approaches could lead to good agreement with the experimental water-surface profiles, their predicted pressure records were overlain with significant fluctuations associated with the particle description of the flow.

The aim of the present study is (1) to provide a clean physical flip-through impact on a realistic coastal structure, that resembles the nature of the classical flip-through impact of Cooker and Peregrine [1]; (2) to reproduce the physical impact numerically with a model similar to that of Cooker and Peregrine [1] and (3) to assess the level of agreement between physical reality and the computational description. Whilst aiming for a high degree of practical relevance, the situation is idealised in a number of ways. In the physical model, for example, history effects are reduced by using an optimised focused wave group to produce a wave with as steep a front as possible when the impact occurs but without visible entrainment or entrapment of air.

The numerical reproduction of the physical conditions is achieved through linear reflection analysis of wave gauge measurements and subsequent application of a fully nonlinear potential-flow solver. The program is an extended version of the one of Cooker and Peregrine [1], where a Schwarz–Christoffel conformal mapping procedure has been added to allow for the piece-wise linear shape of the mound. Furthermore, an ad-hoc wave-generation method has been implemented to enforce the linearly detected incident wave field as boundary condition. The computations are thus also idealised, as they neglect any effects of viscosity, aeration and turbulence.

Given todays computational resources, application of such a potential-flow model is simplistic. The use of a model similar to the one of Cooker and Peregrine [1] however, allows a judgement of how well the potential-flow description of a flip-through impact matches the physical wave impact and establishes a link between the initial theoretical work of Cooker and Peregrine [1] and the experiment. Further, as our interpretation of an ideal flip-through impact implies that no air is trapped or entrained, the impact investigated is likely to be well described by the potential-flow approximation. For the present experiment, we find that this is true for the contraction stage of the impact, while at the point of jet formation, deviations occur. Still, however, the model can give insight into the impact physics. As an example, we find that a reduction of the initial wave amplitudes of only 1.5% leads to a peak pressure reduction of more than 35%, thereby providing a numerical illustration of the strong sensitivity of violent impact pressures to wave shape as reported by e.g. Hattori et al. [3] and Bullock et al. [4].

The experimental setup is described in Sect. 2 and the approach for numerical modelling in Sect. 3. The experimental observations and numerical results are presented and compared in Sect. 4 followed by a summary and discussion in Sect. 5.
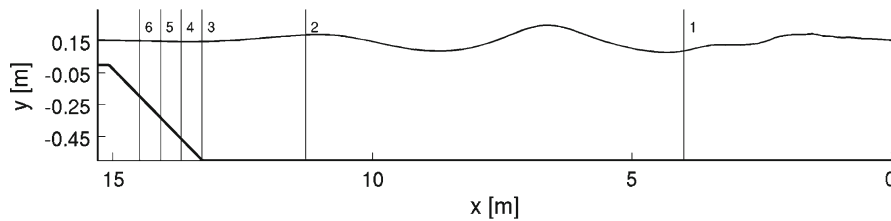
Fig. 1 Wave flume and positions of the six wave gauges. The wave gauges are placed at $x = (4.0, 11.28, 13.28, 13.68, 14.08, 14.48)$ m

2 Experimental setup

The experiments were carried out at the University of Plymouth in a 20.7 m long and 0.9 m wide wave flume equipped with a wedge-shaped paddle. The depth of water was 0.75 m. A sketch of the experimental setup is shown in Fig. 1.

The test structure was intended to represent a typical seawall or caisson breakwater. It consisted of a vertical wall on top of a mound comprising a steep 1:3 slope and a 0.22 m long horizontal berm. The sloping section started 13.28 m from the wave paddle and stretched over a horizontal length of 1.80 m. Consequently there was a still-water depth of 0.15 m on top of the berm and the distance between the wall and the wave paddle was 15.3 m. The slope and berm were constructed from marine plywood while the wall was made from 25.4 mm thick nylon plate. The slope, berm and wall were sealed at the bottom, front and sides in order to minimise the flow of water between the structure and the boundaries of the flume.

The free-surface elevation was measured at 100 Hz by six resistance-type wave gauges placed 4.0, 11.28, 13.28, 13.68, 14.08 and 14.48 m from the wave paddle. At the wall, three FGP XPM-10 pressure transducers were placed 0.10, 0.15 and 0.20 m above the toe of the wall, centered in the lateral direction. A thin layer of Vaseline was applied to the sensors each day before the experiments in order to minimise any thermal shock effects. The pressure data were sampled at 10 kHz using a National Instruments USB-6009 data logger.

The wave motion and impact at the wall was filmed using a NAC HotShot 1280pci high-speed video camera at 500 frames per second and with a resolution of 1280×1024 pixels. The view point was positioned 0.95 m away from the window in the side of the flume. The camera axis was horizontally aligned both normal to the window and along the plane of the wall 0.15 m above the berm.

2.1 Wave generation

The impacting waves were generated using the focused-wave group technique. Focused wave groups have been used as a model for extreme waves in deep water for a number of years, as the technique enables large-amplitude waves to be produced 'on demand' at both a given time and location. The large-amplitude waves are placed within a wave group with an envelope that decays rapidly to zero away from the group centre. This leads to a localised occurrence of one or more extreme waves. For studies of wave-structure interaction, focused wave groups have the advantage of giving an extreme wave event with almost no pre-history of preceding waves.

While initially developed for deep-water experiments, in recent years the focused-wave group technique has been adopted for experiments in intermediate and shallow water. Hunt [14] studied overtopping at coastal structures from storm waves using the focused-wave technique and Katsardi and Swan [15] compared the evolution of focused wave groups in shallow water with those in deep water. Relative to deep water, the effect of nonlinearity is stronger in shallow water and the frequency dispersion is weaker. Although both of these effects act to influence the behaviour of the focusing wave group, the technique is still useful for producing extreme events in intermediate and shallow water.

For the present experiments, the waves were generated using a JONSWAP spectrum [16] with a peak period of 1.984 s. The peak period corresponds to a dimensionless wave number of $kh = 1.32$ in the constant-depth region of the flume. The choice of spectral content gives some control over the shape of the generated focused group, in terms of the number and size of significant waves in the group. The chosen JONSWAP spectrum enabled a small group of about five waves to be generated. The focus location was optimised using an iterative procedure involving the observation of video records from 15 trials, with a requirement for the first significant wave of the group to produce a clean flip-through impact with as steep a wave front as possible but yet with no entrapment or entrainment of air. On the basis of linear constant-depth theory, the results presented later in this paper were obtained using a focus location 16.7 m from the wave paddle. The fact that this placed the nominal focus point behind the seawall illustrates the way focused-wave groups can be used as a practical technique for achieving waves at the required stage of breaking even though their behaviour does not match the linear, constant-depth description associated with the theory.

3 Numerical models

The numerical reproduction of the experimental flip-through impact was achieved by combination of a linear wave analysis model for wave detection and a fully nonlinear potential-flow solver for wave transformation and impact. Both models are described in this section, followed by a description of their combined use.

3.1 Linear wave analysis

In the constant-depth section of the flume, the wave amplitudes are small enough that linear wave motion can be assumed. Below is derived a model for the separation of incident and reflected wave fields, following the early work of Goda and Suzuki [17] and Mansard and Funke [18]. The wave field at any location can be described by Fourier decomposition

$$\eta(x,t) = \sum_{p=1}^{N} \hat{\eta}_p(x) e^{ip\omega t} + \text{c.c.} \tag{1}$$

Here η is the free-surface elevation, measured upwards from the still-water level, N is the number of frequency components, ω is the angular frequency of the first Fourier component and t is time. Next, by assuming that:

1. the wave field consists of a series of linear incident waves and a series of linear reflected waves which do not interact in the region between the wave gauges used in the analysis;
2. the phase variation of $\hat{\eta}_p(x)$ is purely linear;
3. changes in wave amplitude at each frequency is solely due to linear shoaling,

the wave field can be written as

$$\eta(x,t) = \sum_{p=1}^{N} \left\{ A_p^I \left(\frac{c_{g,p}}{c_{g0,p}} \right)^{-1/2} e^{i(p\omega t - \int_0^x k_p dx)} + A_p^R \left(\frac{c_{g,p}}{c_{g0,p}} \right)^{-1/2} e^{i(p\omega t + \int_0^x k_p dx)} + \text{c.c.} \right\} \tag{2}$$

where (A_p^I, A_p^R) are the complex wave amplitudes for the incident and reflected wave components at frequency p; k_p is the linear wave number given by the linear dispersion relation $(p\omega)^2 = gk_p \tanh(k_p h)$; h is the undisturbed depth in the wave flume; $c_{g,p} = \partial\omega/\partial k$ is the group velocity at $k = k_p$ and $c_{g0,p}$ is the group velocity at $x = 0$. The factor involving the group velocities in (2) takes into account linear shoaling of the wave amplitudes due to changes of depth, as shown for example in Dean and Dalrymple [19]. Matching (1) and (2) gives the following relationship between the wave amplitudes and the Fourier coefficient of the time series at the location of wave gauge j

$$A_p^I \left(\frac{c_{g,p}^{(j)}}{c_{g0,p}} \right)^{-1/2} e^{-i\int_0^{x_j} k_p dx} + A_p^R \left(\frac{c_{g,p}^{(j)}}{c_{g0,p}} \right)^{-1/2} e^{i\int_0^{x_j} k_p dx} = \hat{\eta}_p^{(j)}. \tag{3}$$

For M wave gauges, this constitutes M linear equations for the two unknowns (A_p^I, A_p^R) at each frequency. These equations are solved by the linear least squares technique to provide the wave amplitudes (A_p^I, A_p^R).

3.2 Fully nonlinear potential-flow model

The 2D-flow in the wave flume can be considered irrotational and inviscid to a good approximation. This allows the use of potential theory for incompressible flow. As the idealised flip-through impact does not involve entrainment or entrapment of air, incompressible potential-flow theory can also be applied to the impact. In this approximation the effect of the escape flow of the surrounding air is not taken into account and the atmospheric pressure is assumed to be constant. Surface tension effects are also neglected.

A fully nonlinear potential-flow solver, based on the periodic flow program of Dold and Peregrine [20], see also [21], was applied. The extension to a finite domain is presented in [22] and the incorporation of non-uniform depth through conformal mapping is described by Cooker [23]. In the present study the program was extended with a conformal mapping routine that allows the inclusion of a piece-wise linearly shaped mound at the sea bottom. Below is given a brief account of the numerical method, to provide the background for the description of the new conformal mapping.

The free surface is discretised by a set of Lagrangian points for which the position and velocity potential are time stepped using the equations

$$\frac{D\mathbf{X}}{Dt} = \mathbf{U} \tag{4}$$

$$\frac{D\phi}{Dt} = \tfrac{1}{2}\mathbf{U}\cdot\mathbf{U} - p/\rho - gY \tag{5}$$

where $\mathbf{X} = (X, Y)$ is the position of the points, $\mathbf{U} = (U, V)$ is the velocity, ϕ is the velocity potential of the points, p is the fluid pressure, which is set to zero at the free surface, g is the acceleration due to gravity and D/Dt is the material derivative. The velocity $\mathbf{U}$ is found from the surface potential ϕ by solving a boundary-integral equation for the normal derivative of the velocity potential in the complex plane. The free surface is parameterised by the curve $z = R(\xi)$ in the complex plane where ξ is a running parameter. The complex velocity $Q = u - iv$ is expressed in terms of the tangential and normal derivative of the surface potential

$$Q(\xi) = \left(\phi_\xi - i\phi_\nu\right)\frac{R_\xi^*}{\left|R_\xi\right|^2}, \tag{6}$$

where $\phi_\nu = \phi_n|R_\xi|$ is a scaled version of the normal derivative of the potential at the free surface. For a flat sea bed placed in $z = -ih$, the condition of no flux through the sea bed is ensured by adding a mirror image of the velocity field satisfying

$$Q(R^* - 2ih) = Q^*(R). \tag{7}$$

Given the existence of a complex velocity potential $f = \phi + i\psi$ that satisfies $\frac{df}{dz} = Q = u - iv$, $Q(\xi)$ is an analytic function and its value at any point on R can be expressed in terms of the principal value of Cauchy's integral theorem

$$Q(\xi) = \frac{1}{\pi}\oint_C \frac{Q(\xi')}{R(\xi') - R(\xi)}dR', \tag{8}$$

where C is the closed contour consisting of the free surface R, its mirror image through the sea bed and the two vertical strips connecting R and its mirror image at $x = \pm\infty$. As no flow is assumed in the far field these strips do not contribute to the integral. Furthermore, the contribution from the mirror image of R can be expressed solely in terms of the values at R through (7). Insertion of (6) and taking the real part leads to (see [22]):

$$\pi\phi_\nu = \int_{-\infty}^{\infty} \mathfrak{Re}\left\{\frac{R_\xi}{R^{*\prime} - 2ih - R} - \frac{R_\xi}{R' - R}\right\}\phi_\xi'd\xi' - \int_{-\infty}^{\infty}\mathfrak{Im}\left\{\frac{R_\xi}{R^{*\prime} - 2ih - R} + \frac{R_\xi}{R' - R}\right\}\phi_\nu'd\xi'. \tag{9}$$
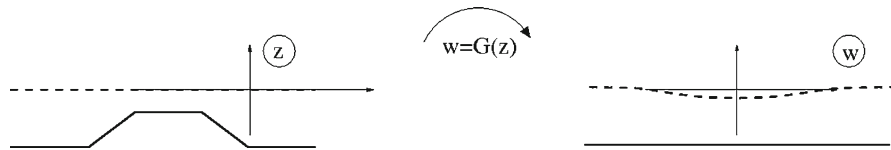
Fig. 2 Conformal map from physical z-plane to w-plane with horizontal sea bed

Given the surface values of R and ϕ_ξ, these integrals can be expressed by quadrature, thus giving a set of discretised linear equations for the determination of ϕ_ν. Special care is needed where R and R' coincide; see [23] and [24]. Once ϕ_ν is known, the velocity of each particle at R can be found through (6). High numerical accuracy is achieved by using high-order discretisation in space and by solving not only for $\nabla\phi$ but also for its time derivatives. This allows time stepping of (4)–(5) through the explicit Taylor expansion in time. Both aspects are detailed in [21].

The above procedure allows for a horizontal sea bed. An irregular sea bed can be treated by conformal mapping. Suppose a conformal mapping $w = G(z)$ exists, that maps the physical domain z with an irregular sea bed to a domain w with a flat sea bed. Now as the mapping is conformal, the potential $f(z)$ also satisfies the Laplace equation in the w-plane. The velocities in the z plane and w plane are connected through

$$Q = \frac{df}{dz} = \frac{df}{dw}\frac{dw}{dz}. \tag{10}$$

Hence to solve for the wave evolution over an uneven sea bed, we can, in each time step, map the free surface into the w-plane where the image of the sea bed is a straight horizontal line. The velocities at the free surface in the w-plane can next be found by solving an integral equation equivalent to (9) in the w-plane. Finally the velocities at the free surface in the physical plane are found through (10) and (4)–(5) can be time stepped similarly as for a flat sea bed. This technique was applied by Cooker et al. [23] to model wave transformation over cylindrical obstacles at the sea bed.

3.3 Conformal map for a piece-wise linearly shaped sea bed

We here describe a conformal mapping that maps a piece-wise linear sea bed shape into a horizontal line, as shown in Fig. 2. This mapping is needed for the numerical description of the mound shape of the experiment. In the numerical computations, the effect of the wall is simply mimicked by mirroring the domain to achieve symmetry across the wall. For this reason the mound shape depicted in Fig. 1 results in a map like the one sketched in Fig. 2, that contains the full mirrored representation of the physical mound.

The basis is the Schwarz–Christoffel transformation

$$z = z_0 + c \int_0^q (1 - q/q_1)^{\beta_1} (1 - q/q_2)^{\beta_2} \ldots (1 - q/q_N)^{\beta_N} \, dq \tag{11}$$

that maps the interior of the complex unit circle into the interior of a closed polygon as illustrated in Fig. 3. The transformation is defined by the *image points* $(z_1, \ldots, z_N)$ with associated angle parameters $\beta_1, \ldots, \beta_N$, which are measured in the image plane as the outer angle at each corner of the polygon, divided by $-\pi$. This is illustrated for β_3 in the figure.

Usually, the image points $(z_1, \ldots, z_n)$ are known, while the *prevertices* $(q_1, \ldots, q_N)$, the scaling factor c and z_0 (the image of $q = 0$ in the polygon) must be found by solving a system of nonlinear equations.

The polygon may be degenerate, i.e., one of the corners may be placed at infinity. An example is shown in Fig. 4, where the unit disk is mapped onto the complex half-plane above a curve composed by segments of straight lines. The image point z_4 is placed at $z = \infty$. For such a corner, $\beta = -2$.
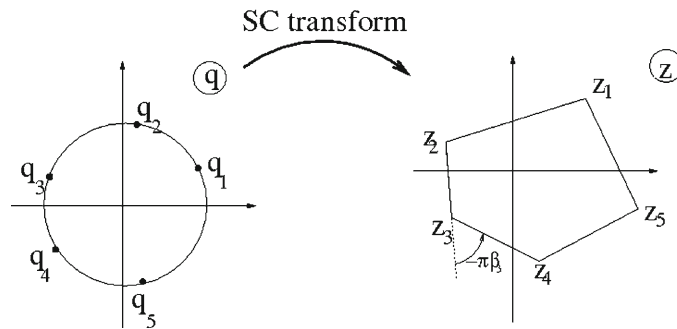
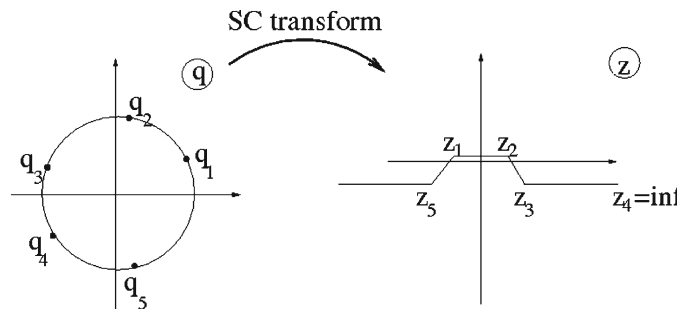**Fig. 3** Example of a Schwarz–Christoffel transformation

Fig. 4 Example of a Schwarz–Christoffel transformation with degenerate polygon

A mapping of this type is the main ingredient of the full transformation from the piece-wise irregular sea bed to a flat sea bed. The full transformation implemented is illustrated in Fig. 5 and consists of the following five steps:

Step 1 (translation): $\qquad\qquad\qquad\qquad \tilde{z} = z - x_c$ (12)

Step 2 (mapping to unit disk): $\qquad\qquad q = \text{SC backward}(\tilde{z})$ (13)

Step 3 (rotation): $\qquad\qquad\qquad\qquad \tilde{q} = q/q_{N-1}$ (14)

Step 4 (mapping to upper half-plane): $\quad \tilde{w} = i\dfrac{1 + \tilde{q}}{1 - \tilde{q}}$ (15)

Step 5 (translation): $\qquad\qquad\qquad\quad w = \tilde{w} - ih$ (16)

Step 1 centres the bed variation horizontally. Step 2 transforms the polygon-shaped sea bed in $\tilde{z}$ to the unit circle in the complex plane. Step 3, the rotation, maps q_{N-1} to $\tilde{q}_{N-1} = 1 + 0i$, ensuring that the original real axis in the z-plane is mapped onto a horizontal line in the $\tilde{w}$ plane. The transformation in step 4 is called the Mobius transformation and maps the interior of the unit disk onto the upper complex half-plane. Step 5 moves the mapped sea bed down such that it is mapped onto points of vertical level $-ih$.

The derivative, dw/dz, which is needed for evaluation of (10) is obtained as follows

$$\frac{dw}{dz} = \frac{d\tilde{w}}{d\tilde{q}} \frac{d\tilde{q}}{dq} \frac{dq}{d\tilde{z}} = \frac{d\tilde{w}}{d\tilde{q}} \frac{d\tilde{q}}{dq} \frac{1}{\frac{d\tilde{z}}{dq}}, \tag{17}$$

where

$$\frac{d\tilde{w}}{d\tilde{q}} = i\frac{2\tilde{q}}{(1 - \tilde{q})^2}, \tag{18}$$

$$\frac{d\tilde{q}}{dq} = 1/q_{N-1}, \tag{19}$$

$$\frac{d\tilde{z}}{dq} = c\,(1 - q/q_1)^{\beta_1}\,(1 - q/q_2)^{\beta_2}\dots(1 - q/q_N)^{\beta_N}. \tag{20}$$

The numerical implementation of the conformal map is based on the Fortran library SCPACK of Trefethen [25]. This library contains subroutines that set up the Schwarz–Christoffel transformation (11) by solving a set of nonlinear equations for the unknowns $c, q_0, \ldots, q_N$. Subroutines that perform the forward and backward transformations are also supplied.

3.4 Combined use of the two models

The linear wave-analysis model and the fully nonlinear potential-flow model were combined to reproduce the laboratory wave impact.

First the linear analysis model was used to determine the complex amplitudes of the incident wave field. Due to the linear approximations of this model, the bound waves at the sum and difference frequencies could not be detected. Schäffer and Steenberg [26] provide a detailed account of the components of the second-order field produced when, as in the present case, a wave paddle is only moved in accordance with linear theory. Among these are (1) the second-order bound waves generated by the interaction of the linear free wave components and (2) a matching set of free waves that act to cancel the motion of the bound waves at the wave paddle position. An analysis of the long second-order waves associated with propagation of focused wave groups can be found in Hunt et al. [27].

An accurate description of the long second-order waves is important when modelling violent wave impacts due to the fact that the impact type is strongly sensitive to the local depth at the wall, see for example Peregrine et al. [28]. To achieve this, the fully nonlinear potential-flow model was run with the incident linear wave field imposed as a boundary condition at the position of the wave paddle, i.e., at $x = 0$. The choice of a numerical wave-generation location that coincides with the physical one and the numerical enforcement of purely linear wave motion allows for direct numerical modelling of the second-order wave components (1) and (2) as described above. We note that this procedure may not capture the full second-order wave field as, for example, the bound progressive second-order waves associated with interaction of first-order evanescent wave modes in the vicinity of the wave paddle are not modelled; see [26]. Nevertheless, the procedure was considered a reasonable approach for transferring the linear wave field to the nonlinear model and produced better results for the second-order long waves than an alternative procedure in which the linear wave field at a particular instant of time was imposed as initial condition for the computation.

In the fully nonlinear potential-flow solver, the linear incident wave field was enforced by an ad-hoc procedure, where the source terms

$$Y_t = \gamma(Y_{\text{computed}} - Y_{\text{target}}), \tag{21}$$
$$\phi_t = \gamma(\phi_{\text{computed}} - \phi_{\text{target}}), \tag{22}$$

were added to the right-hand side of the governing equations (4)–(5) within a relaxation zone stretching three wave lengths to the offshore from the wave maker position at $x = 0$. Here Y_{computed} is the result for Y that the potential-flow model produces, Y_{target} is the value of Y according to the extracted linear incident wave field and $\gamma = -10$. This choice of γ was found to provide satisfactory results for the wave generation, and no further optimisation of the parameter was pursued. For a constant value of Y_{target}, (21) in isolated form has the solution $Y = Y_{\text{target}} + [Y_{\text{initial}} - Y_{\text{target}}] \exp(\gamma t)$ and thus imposes an exponential decay towards $Y = Y_{\text{target}}$. In combination with the potential-flow model (4)–(5), the source terms act to enforce the values of the target solution within the relaxation zone. Given the ad-hoc nature of the source terms, their time stepping was simply performed to first-order accuracy, after each time step of (4)–(5). For Y this results in the update scheme

$$Y_{\text{updated}} = Y_{\text{computed}} + \Delta t \gamma(Y_{\text{computed}} - Y_{\text{target}}), \tag{23}$$

which by substitution of $\alpha = -\Delta t \gamma$ can be written as

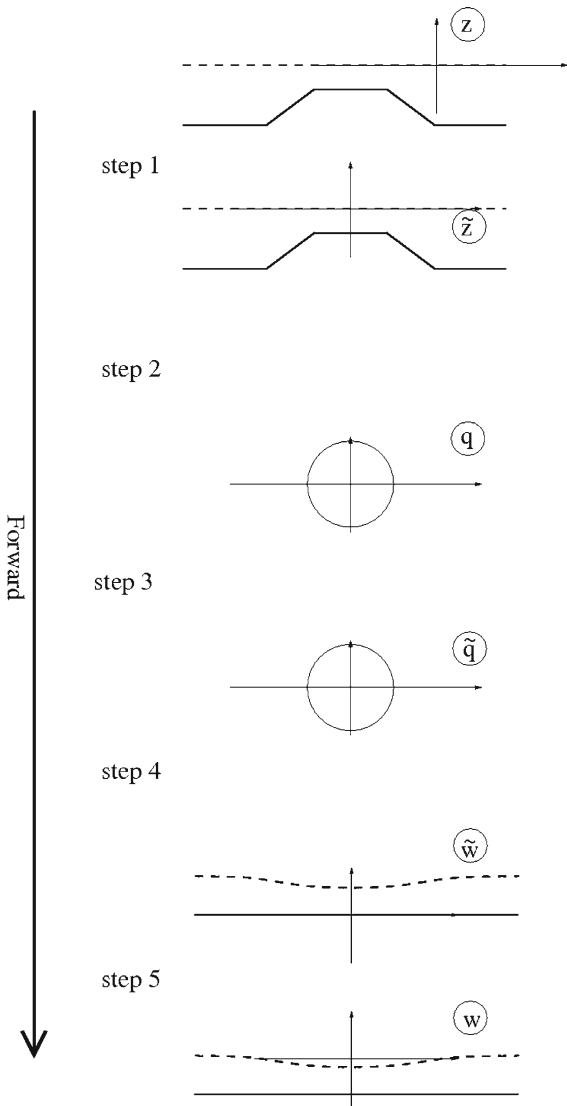$$Y_{\text{updated}} = \alpha Y_{\text{target}} + (1 - \alpha) Y_{\text{computed}}. \tag{24}$$

Fig. 5 Steps in the transformation from a piece-wise linear sea bed to uniform depth. The steps of *1* (translation); *2* (mapping to unit disk); *3* (rotation); *4* (mapping to upper half-plane) and *5* (translation) are described in (12)–(16)
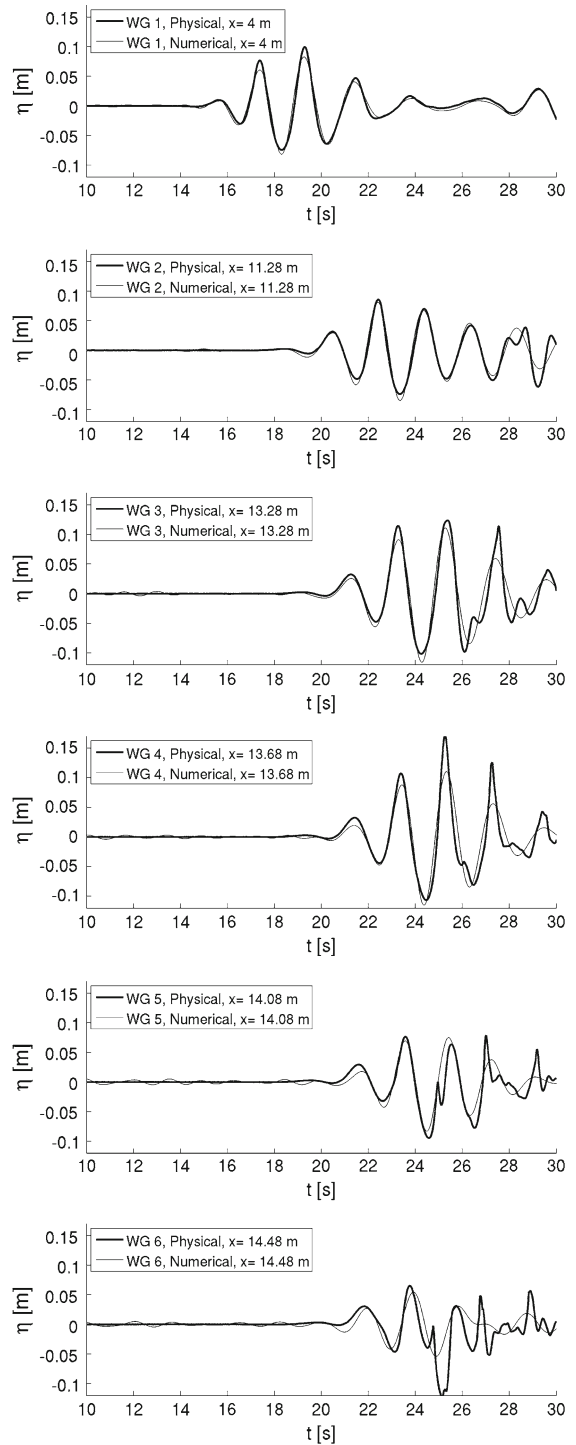

Fig. 6 Surface elevation at the wave gauges and reproduction by linear analysis

The latter formula is well established for wave generation in Boussinesq models, see for example [29] where, however, α is usually chosen to vary smoothly from unity at the offshore end of the wave-generation zone towards zero at the landward end. The purpose of this is to provide a soft transition from enforcing the target solution inside the generation zone to the wave models description of the flow outside the generation zone. For the present purpose, however, where the second-order waves emerge due to a mismatch between the imposed linear wave motion and the fully nonlinear wave behaviour, a distinct border between the wave-generation zone and the domain of free wave propagation is needed. For this reason a constant value of $\gamma = -10$ was applied all the way up until $x = 0$.

4 Experimental observations and numerical results

4.1 Wave gauge records and results of linear analysis

Time series of the free-surface elevation from the six wave gauges depicted in Fig. 1 are presented in Fig. 6, together with results of the linear wave analysis. We first discuss the experimental data.

At wave gauge 1 ($x = 4$ m), the incident waves are well separated in time from those subsequently reflected from the structure. This enables the form of the incident group to be clearly seen between $t = 14$ s and $t = 26$ s. By gauge 2, which is much closer to the structure ($x = 11.28$ m), the incident and reflected waves overlap. This overlap occurs to an increasing extent for the remaining wave gauges. At wave gauges 5 and 6 ($x = 14.08$, 14.48 m), the variation in water surface elevation is smaller than at the earlier wave gauges. This is due to the fact that, in this region, the incident and reflected waves to a large extent have opposing amplitudes and therefore partially cancel each other out, while the opposite effect causes positive interference in the vicinity of wave gauges 3 and 4.

In the linear separation model, the surface motion is decomposed into an incident and reflected amplitude at each frequency. Data from the first four wave gauges only were used, as the last two wave gauges were placed at relatively shallow water depths, where the assumption of linear motion may not be valid. A frequency interval of $f = [0.20;\ 0.82]$ Hz was chosen for the analysis, based on inspection of the raw amplitude spectra from the wave gauges. An example of this is shown in Fig. 7 for the third wave gauge. The main spectral peak is located within the frequency interval mentioned, with bound wave energy visible outside this range at the double peak frequency and at the difference frequencies. Figure 6 indicates that the linear analysis model successfully captures the overall motion at all of the first four gauges although the peaks of the wave crests are not fully reproduced, especially at gauge 4. Likewise, the size of the first significant wave trough is over-estimated at the first four gauges. Both effects are a clear sign of missing second-order harmonics in the linear description. At the final two gauges, the linear model offers a surprisingly accurate description of the first two wave crests but there are significant discrepancies during the remaining part of the record. The second wave, which occurs just before $t = 24$ s at gauge 6, is the one that produces the flip-through impact at the wall. The reflection and other interactions from this impact gives rise to the irregular behaviour seen in the physical record after $t = 25$ s and which the linear numerical model is unable to reproduce.
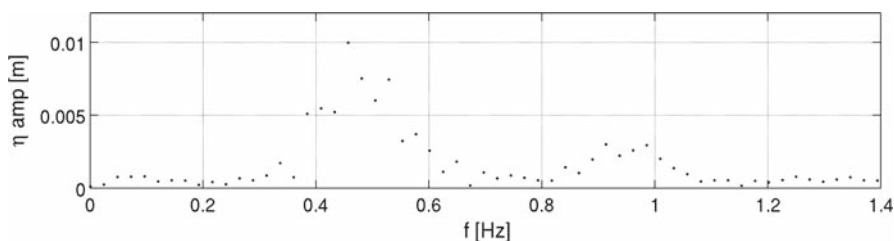

Fig. 7 Raw amplitude spectrum of surface elevation record from wave gauge 3 at $x = 13.28$ m

4.2 High-speed video of the impact

High-speed video images of the flip-through impact are presented in Figs. 8 and 9. No corrections have been made for the effects of perspective, which explains why the front of the wave can be seen across the whole width of the flume as the wave approaches the wall. This view provides information on the extent of transverse non-uniformities.

The first column of Fig. 8 shows the waves approaching the wall, with 40 ms between each frame. The wall is seen at the left of each frame with three horizontal lines that mark the position of the pressure transducers 0.1, 0.15 and 0.20 m above the toe of the wall. The upper corner of the berm is visible in the lower right-hand side region of the frames, giving an impression of the physical scale. The free surface is seen to be very smooth, the first small wave of the group having caused little disturbance when it reflected gently from the wall. In the two last frames of the column, transverse deviations are seen. In particular we note that the wave profile is slightly overhanging at the centre-line of the flume, contrary to the profile adjacent to the window.

Details of the impact are shown in the second column of Fig. 8 and in Fig. 9 with steps of 4 ms between each frame. In the second column of Fig. 8 the final approach of the wave front to the wall is shown. Simultaneous vertical movement of the free-surface intersection point with the wall can also be seen. The images in the first column of Fig. 9 cover the emergence of the vertical jet. Strong vertical acceleration of the water level in the trough point can be seen, leading to a complete in-filling of the initial gap between the wave front and the wall. The jet emerges at $t = 23.889$ s. Further evolution of the jet is shown in the last column of the figure which also shows how the jet breaks up into droplets.

From the frames of $t = 23.881, 23.885$ and 23.889 s, the impact is seen to take place just below the still-water level at $z = 0.15$ m. This is in contrast to the observations of Hull and Müller [10] and Lugni et al. [11] who both reported that the high-pressure region occurred above still-water level. In practice, the impact location depends on the wave shape which in turn generally depends on the bathymetry. The flip-through impact simply requires the correct balance between the horizontal motion of the wave front and the vertical motion in the wave trough to occur. Hence the precise elevation of the high-pressure zone is case specific.

4.3 Fully nonlinear potential-flow computations for wave transformation and impact

The fully nonlinear potential-flow solver enables nonlinear wave transformation along the wave flume and over the mound as well as the flip-through impact process to be modelled. The predicted variations in water surface elevation at the six wave gauges are shown in Fig. 10 and compared to the experimental data. The numerical impact takes place at $t = 23.881$ s at which time the numerical computation terminates. In general the numerical results up until this instance in time are in much better agreement with the physical data than the linear model results of Fig. 6. However, the nonlinear model accentuates the low-amplitude oscillations in front of the main waves that it inherits from the linear model (see Fig. 6) and it overestimates the elevation of the preceding trough of the impacting wave at gauge 6.

Spatial profiles of the free surface up to the occurrence of the flip-through impact are shown in Fig. 11a with jumps of 0.1 s. Close to the wall, the last profile closely resembles a quarter-circle, as can be seen in Fig. 11b and in Fig. 8 for $t = 23.849$ s.

The computational flip-through impact is compared to the experimental one in Figs. 12 and 13, where the numerical solution for the free-surface position has been overlaid onto the video frames of Figs. 8 and 9. These figures can therefore be cross-referenced when examining the match of the numerical solution to the experimental results. The numerical computation broke down during impact while the vertical jet was emerging; comparisons beyond $t = 23.881$ s are therefore not presented.

When conducting the experiment, the trigger signal for the camera was logged together with the wave data and the pressure data. This allowed synchronisation of the pressure data, wave data and video frames. Synchronisation with the numerical results was also possible, as these are driven by the wave data. By comparison with the video images, however, the best agreement was found by subtraction of a time shift of 0.021 s
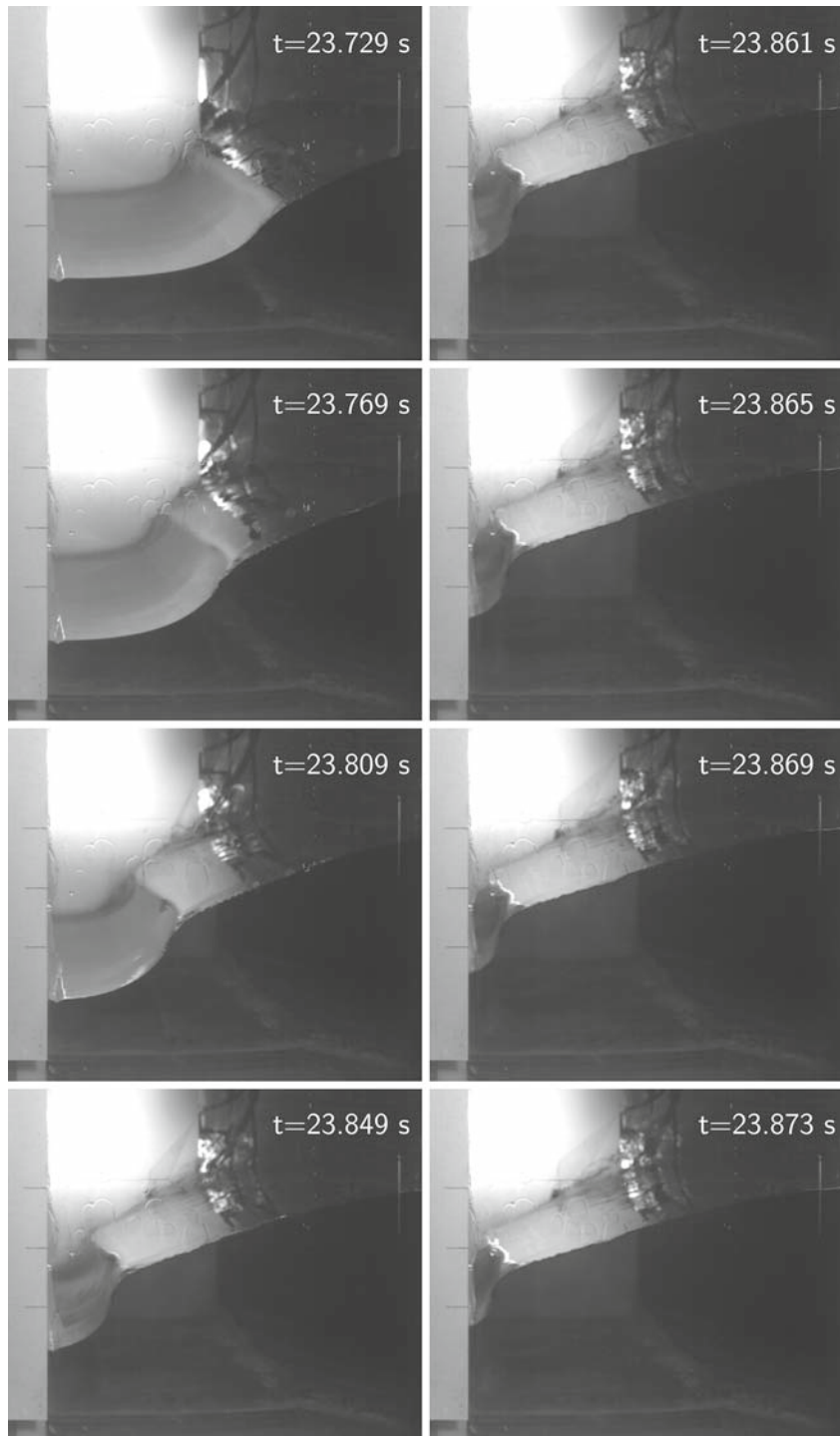
Fig. 8 High-speed video images for the flip-through impact. Timings for each image are given in the top right corner

from the numerical time. This is about double the synchronisation uncertainty associated with the sampling rate of 100 Hz for the wave data, and may be attributed to a slight deviation in the travel time from the wave paddle to the vertical wall between the experiment and numerical computation. The numerical data have been
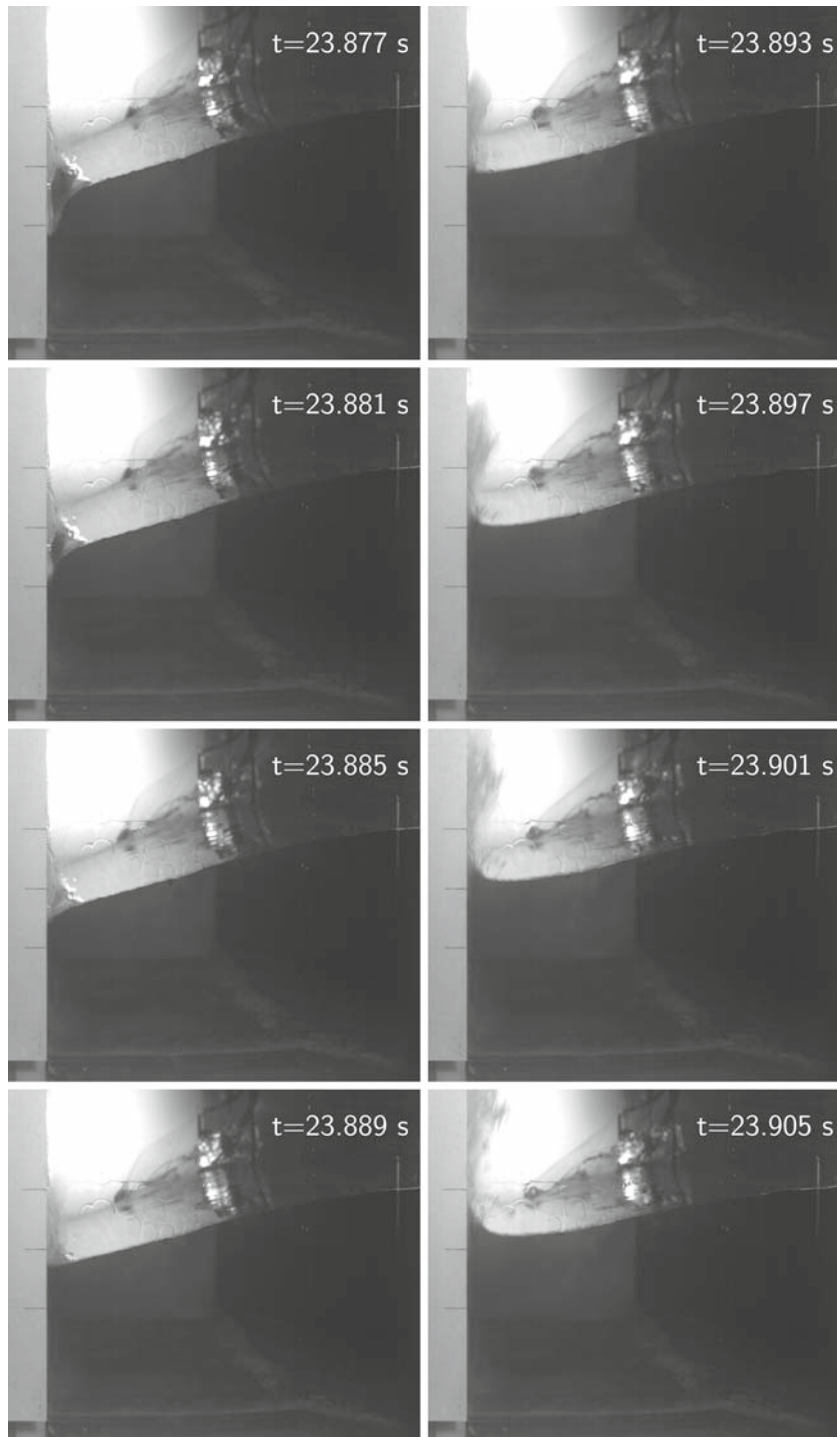
Fig. 9 High-speed video images for the flip-through impact. Continued from Fig. 8

corrected with the mentioned time shift, such that all timings quoted in the paper refer to the experimental time.

The first column of Fig. 12 shows the initial approach of the wave leading up to the impact. Apart from a slight overall vertical shift of the surface profile, there is good agreement between the numerical solution and
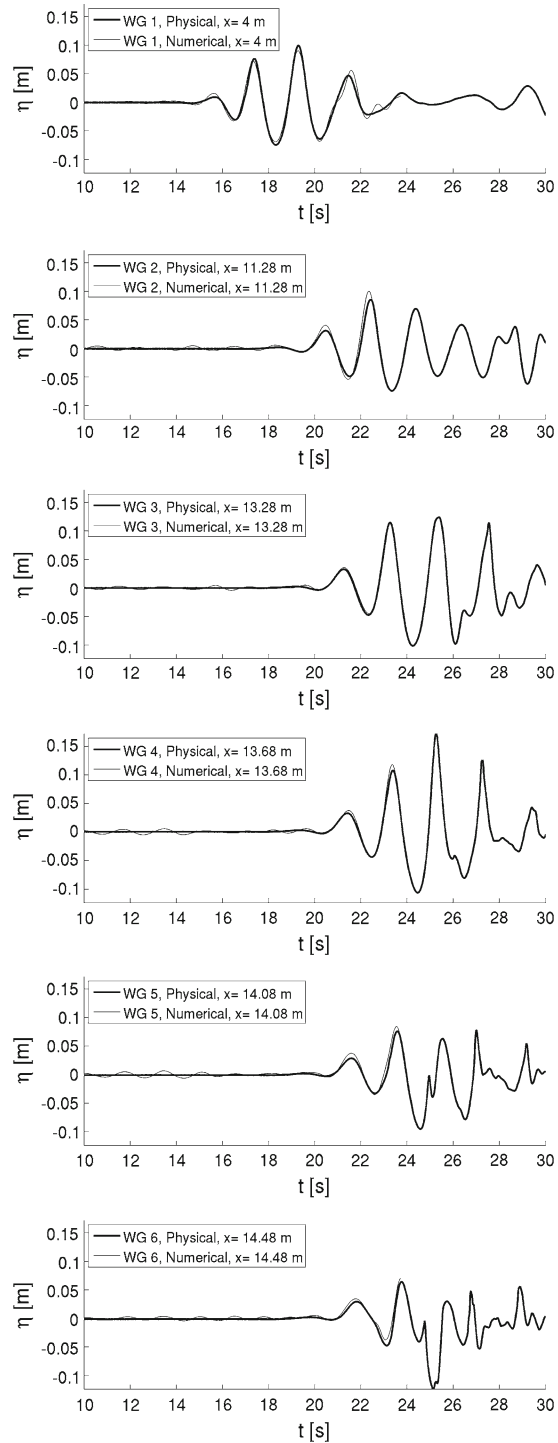
Fig. 10 Surface elevation at the wave gauges and results of fully nonlinear potential-flow computations
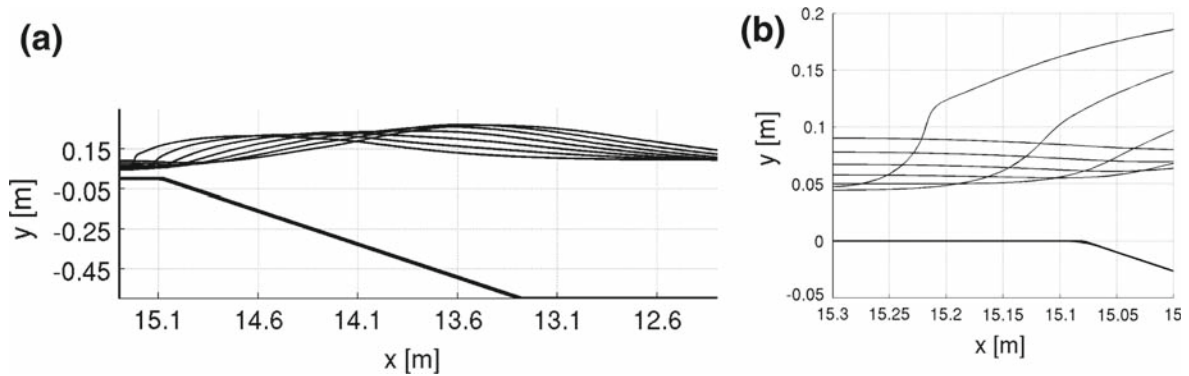
Fig. 11 **a** Snapshots of surface profiles for $t = (23.229, 23.329, \ldots, 23.829)$ s up to the time of the flip-through impact, obtained from fully nonlinear potential-flow computations. **b** Close-up of region close to the wall

the free surface adjacent to the window of the tank. Further progress towards impact is shown in the second column. As discussed in relation to Fig. 8, transverse variation of the wave front position occurs at this stage and the experiment is therefore not purely two-dimensional. The target position of the numerical results is thus less well defined at this stage. To avoid the effects of perspective mentioned previously, all the numerical predictions are compared with the free surface of the water adjacent to the inside of the window. At this lateral position, the numerical model is able to reproduce the focusing of the profile. The overall vertical shift is reduced and excellent agreement between the numerical solution and the experiment is seen in the last column of the figure and in Fig. 13.

Just after $t = 23.877$ s the flip-through of the numerical solution occurs. A vertical jet emerges from the wave trough adjacent to the wall, between the wall and the wave front. The jet is visible in the last frame of Fig. 13. The computation was unable to continue after this time, as the top of the jet motion moved towards a backward impact with the advancing wave front, as can be seen in Fig. 16a.

The emergence of the jet inside the gap between the wall and the wave front is markedly different from the evolution of the physical wave at $t = (23.885, 23.889, 23.893)$ s in Fig. 9, where the jet is only formed after the gap between the wave front and the wall has been filled with water. Also, the upward jet in the experiment consists of spray and droplets, which is very different from the potential-flow description of a single-connected single-phase fluid. Hull and Müller [10] also found that the jet in their flip-through impact did not emerge between the wave front and the wall, but occurred after the gap was filled by water.

4.4 Impact pressures

The pressure time histories from pressure transducers 1 and 2, placed 0.10 m and 0.15 m above the toe of the wall, are shown in Fig. 14. The plot also show the impact pressures of the next wave in the group at about $t = 25.9$ s. The third pressure transducer at $z = 0.20$ m was largely out of the primary impact zone and has been omitted for clarity. The overall pressure history is typical for a violent impact; see, for example, [3] and [4]. It shows a marked peak at impact, with a maximum pressure of 21.2 $\rho g h_{\text{wall}}$, where $h_{\text{wall}} = 0.15$ m is the still-water depth at the wall. There is a sharp rise towards this peak which indicates that the strong impact pressure is not associated with entrapment of air at the transducer. After the impact peak, a quasi-hydrostatic pressure, about $1.5 \rho g h_{\text{wall}}$ for transducer 1, lasts for about 0.5 s. This is associated with the presence of water running up and down the wall and occurs even for weak reflection of waves at a vertical wall.

A comparison of the experimental and numerical pressure is shown in Fig. 15, which is a close-up of the pressure peak at impact. The numerical pressure is only shown for the lowest pressure gauge at $z = 0.10$ m, as the other
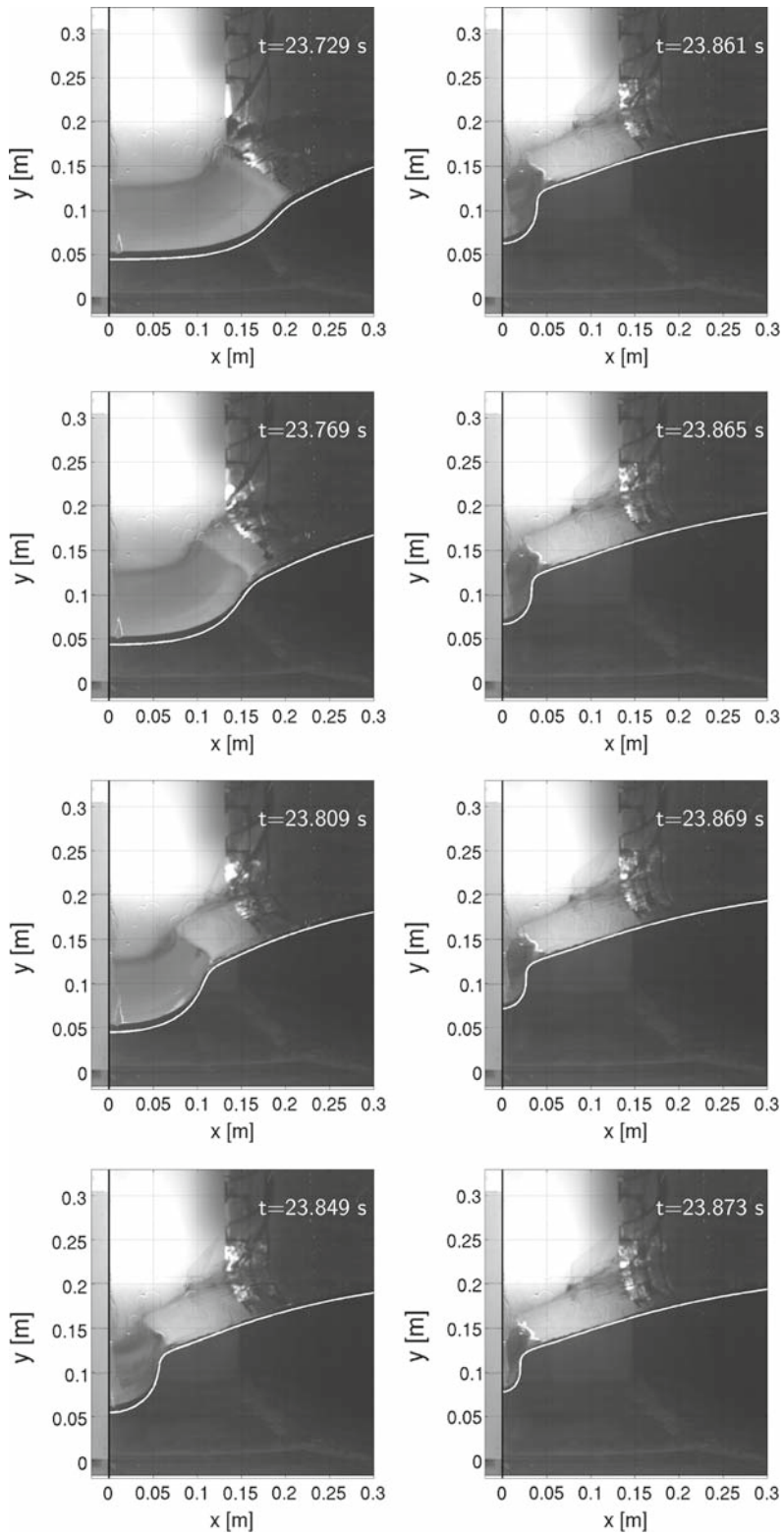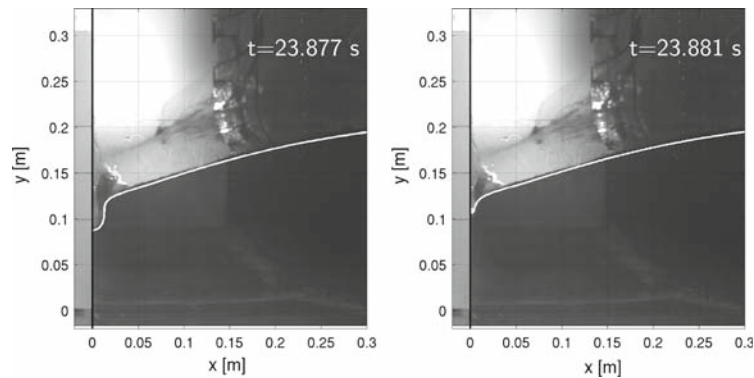
Fig. 12 Video and numerical solution
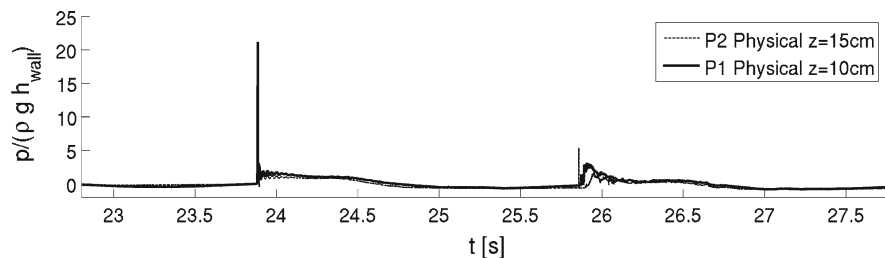
Fig. 13 Video and numerical solution

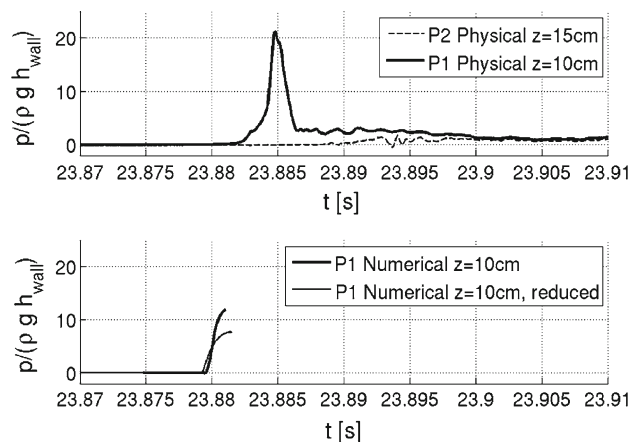**Fig. 14** Time histories of pressure for the physical flip-through impact

Fig. 15 Comparison of physical pressure (upper panel) and numerical pressure (lower panel). Pressure results for the reduced numerical run are shown as a thin line

gauges had not been reached by water at the time where the computation terminated. The numerical pressure shows a steep rise towards a terminal value of 11.94 $\rho g h_{wall}$. Although the slope of the rising numerical pressure is in good agreement with the experimental curve, the potential-flow model is not able to compute the pressure variation through to and beyond the time instant of maximum pressure.

An explanation for the cause of the potential-flow computation break-down is provided by Fig. 16a where consecutive free-surface profiles of the numerical solution are plotted with time increments of 0.2 ms. The contraction of the free-surface profiles is evident and the emergence of the jet at the wall can be clearly seen. In the last three profiles, the top of the jet becomes increasingly wide and develops a 'shoulder' that moves upward and away from the wall. Although the computation broke down shortly after the last of the profiles due to excessive accelera-
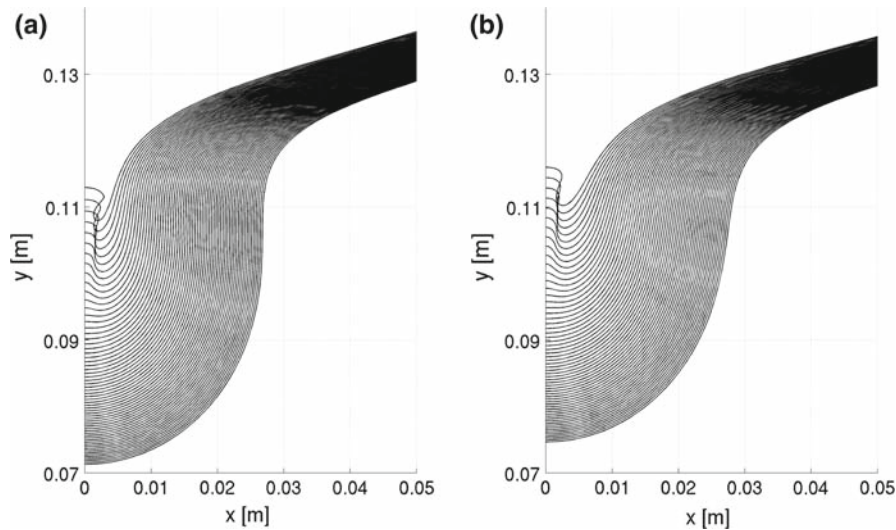
Fig. 16 Consecutive free-surface profiles for the numerical results of Figs. 12 and 13 (**a**) and for the run with reduced amplitudes (**b**). The first profile is for $t = 23.869$ s with a time increment of 0.2 ms between the profiles

tions and curvature of the free surface, it seems that the shoulder approaches a collision with the advancing wave front with subsequent entrapment of an air bubble within the water body. Such a flow formation is clearly beyond potential-flow modelling.

To obtain a numerical flip-through impact that allowed computation through to the time of maximum pressure at $z = 0.10$ m, an additional computation was made, identical to the original one, except for a 1.5% reduction of the incident wave amplitudes for the linear driving boundary condition. The consecutive free-surface profiles leading up to impact are shown in Fig. 16b and have many similarities to the original ones shown in panel (a). The top of the jet, however, does not bounce away from the wall to the same extent as for the original run. At $z = 0.10$ m this impact reached maximum pressure just before termination of the computation. The pressure history is shown in Fig. 15 as a thin line. The rise towards the peak is more gentle and the peak pressure of 7.67 $\rho g h_{\text{wall}}$ is 36% smaller than the terminal pressure of the original run.

As already mentioned, the strongest impact pressures occur for impacts that trap a small pocket of air at the wall [2–4]. Furthermore, for such impacts, the impact type and impact pressures are strongly sensitive to the shape of the incoming wave [3,5,28]. The surface profiles of the original run (Fig. 16a) indicate that the numerical event is close to producing an overturning impact and thus belongs to the category of wave impacts that generate the largest pressures. The strong sensitivity of the impact pressure to wave shape, as illustrated by the run of reduced wave amplitudes, provides support for this assumption. Combined with the visual observation of no entrainment or entrapment of air during impact, the above numerical results indicate that the experimental impact is really an 'ideal' flip-through impact of the largest possible steepness, yet without entrapment or entrainment of air.

Detail of the pressure histories at the wall are shown in Fig. 17 as contour plots of wall pressure in the (t, y)-plane. The instantaneous position of the free surface is marked as a thick line. The figure shows how the pressures of the impact zone are spread down the wall. Although the peak pressure for the two solutions are different, the overall pressure histories at the wall have many similarities. This can be linked to the impulse of the wave impact, which is much more invariant to changes in the shape of the impacting wave than the instantaneous force and pressure; see e.g. [28].

5 Discussion

An experimental and numerical study of the flip-through impact has been carried out for a geometry resembling a typical seawall and with the impacting wave created using the focused-wave group technique. This approach allows
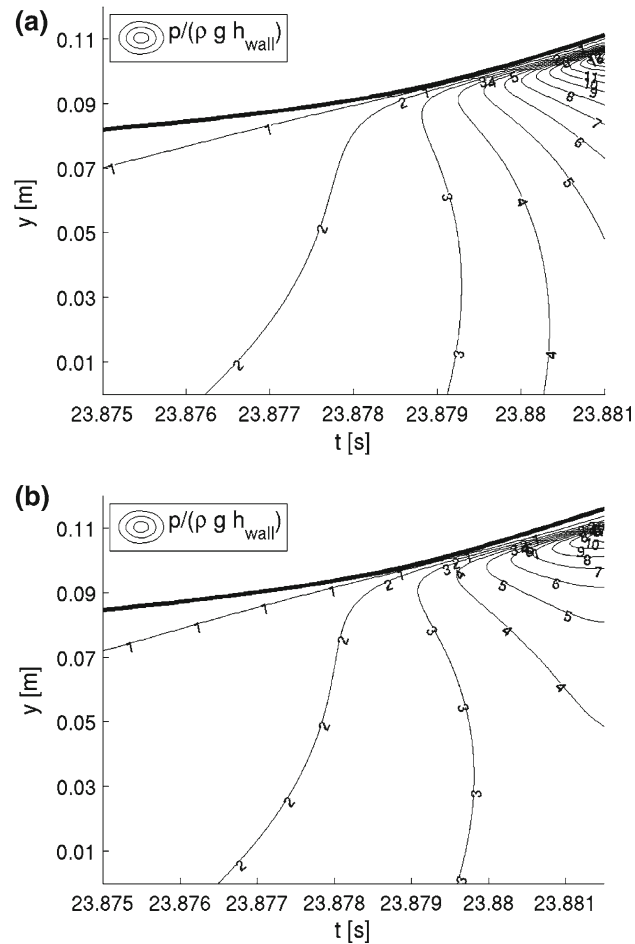
Fig. 17 Pressure at the wall plotted in the (t, y)-plane for the numerical solution of Figs. 12 and 13 (**a**) and for the run with reduced amplitudes (**b**). The numbers on the contours are the pressure in units of $\rho g h_{\text{wall}}$

the generation of a large-amplitude wave with no significant preceding impact. The resulting flip-through impact is therefore practically free from entrained air and free-surface disturbances caused by earlier impacts. An ideal flip-through impact with the largest possible steepness but without entrapment or entrainment of air during impact has been achieved by careful adjustment of the focus location. High-speed video frames of the impact have been shown, providing details of the contraction, impact and rise of the jet. Recorded pressure time histories have been presented, revealing a peak pressure of $21\rho g h_{\text{wall}}$.

The initially smooth surface and absence of previously entrained air makes the resulting impact a perfect candidate for comparison to potential-flow computations of the kind originally presented by Cooker and Peregrine [1]. This has been achieved with the addition of a Schwarz–Christoffel conformal mapping to a fully nonlinear potential-flow solver, which is essentially the same program as that of Cooker and Peregrine [1]. An ad-hoc wave generation method has been implemented, following the lines of the relaxation zone technique, often used in Boussinesq-type wave models. To obtain the incident wave field for the potential-flow solver, a linear analysis method has been developed, following the lines of Goda and Suzuki [17] and Mansard and Funke [18], extended to varying depth.

The results of the linear analysis model offer a fair reproduction of the wave gauge records, although second-order effects are clearly missing. Further computations with the fully nonlinear potential-flow solver show good agreement with the wave gauge data for the impacting wave. The numerical solution for free-surface elevation

during the impact has been overlaid on the high-speed video frames to allow direct visual comparison. Apart from an initial vertical shift of the profile, an excellent match is found, reproducing the contraction of the free surface towards the impact zone. At impact, the numerical solution shows different behaviour compared with the experimental one, in that the vertical jet emerges inside the gap between the advancing wave front and the wall, whereas in the experiment, the jet emerges after infillment of the gap.

The numerical pressures show a similar steepness for the front face of the pressure peak when compared to the experimental results. The computation, however, broke down before maximum pressure was reached. The numerical solution showed that the vertical jet was about to rebound into the approaching wave front, indicating that the numerical impact is at the border of flip-through impact. This was supported by the results of an additional computation with slightly reduced wave amplitudes. The computation demonstrated a strong sensitivity of the wave impact pressures to the shape of the impacting wave, in agreement with the findings of Hattori et al. [3] and Bullock et al. [4].

Some of the differences between the experiment and numerical solution for the emergence of the jet, may be attributed to the strong sensitivity of the impact type to wave shape. It is not unlikely that small errors, induced by the approximations associated with the linear wave separation model, can be responsible for the precise impact type of the numerical computation. Although the numerical solution has provided an excellent match for the free-surface contraction until the development of the jet, the type of impact makes a good agreement during jet formation difficult to achieve.

Three-dimensional effects are also likely causes for the discrepancies, for example through non-uniformity of the impacting wave front across the wave flume. Whilst the video does not show any hint of entrained or trapped air, it is possible that this has happened at other locations across the flume. Indeed the frame of $t = 23.849$ s of Fig. 8 does show more pronounced overturning at the centre of the flume than at the front glass. Hence an impact with a jet formation that resembles the numerical one may have taken place at some cross-flow location in the flume. Bullock et al. [4] found that the violent impact pressures are often non-uniform in the transverse direction for nominally two-dimensional tests.

Another clear source of deviation between the experiment and the computations presented are the inherent assumptions of inviscid, single-phase, single-connected flow of potential theory. At impact where droplets are formed and the fluid separates these assumptions are no longer valid and a close agreement with the experiment cannot be expected. At this stage of jet formation, the flow is really a two-phase flow, where the mixing of water and air becomes important. For the thin jet of the numerical solution seen in Fig. 16, the introduction of viscous effects would result in a strong cross-flow shear, and any mixing in the direction normal to the wall would induce stresses in the vertical direction and strongly perturb the flow. We also note that any exchange of droplets or fluid particles across the gap between the jet and the wave front, where the vertical velocities are very different, would disturb the flow and possibly induce further mixing. It is therefore conceivable that the fine features of the rising jet and narrow air gap of the numerical solution are products of the idealised nature of the potential-flow description.

Besides establishing a clean experimental flip-through impact and reproduce it numerically with a potential flow solver, the purpose of the present study has been to assess the agreement between the physical and computational impacts. Up until the stage of jet formation, the numerical solution matches the experimental results well, and the 'ideal' flip-through impact achieved in the laboratory can thus be viewed as the experimental counterpart of the computational flip-through impact as discovered by Cooker and Peregrine [1]. The effects of two-phase flow with aeration and mixing can be described by more advanced numerical models. Bredmose et al. [5] applied a two-phase flow model to a flip-through impact and to impacts trapping small air pockets, taking the effects of entrained and entrapped air into account. It was found that the border-line between flip-through with no air entrained or trapped, and impacts that entrain a small air pocket is not as sharp as potential-flow computations would suggest. However, apart from the fine details of jet formation and generation of droplets, it is remarkable how close a description of the physics the elegant potential-flow description can offer for impacts that do not entrap air.

experiments were conducted within the OVI research project (Fundamentals of Overtopping from individual Violent water wave Impacts) at the University of Bristol and the University of Plymouth. Howell was leading the research activities at Bristol up until his sudden death in March 2007. We are grateful for many good discussions with Howell and will remember him as a great spirit with a strong mind, always keen to share his enthusiasm for Fluid Mechanics and water waves.

References

1. Cooker MJ, Peregrine DH (1990) Computation of violent wave motion due to waves breaking against a wall. In: Proceedings of the 22nd International Conference on Coastal Engineering. ASCE, Delft, pp 164–176
2. Bagnold RA (1939) Interim report on wave-pressure research. Proc Inst Civil Eng 12:201–226
3. Hattori M, Arami A, Yui T (1994) Wave impact pressure on vertical walls under breaking waves of various types. Coast Eng 22(1–2):79–114
4. Bullock GN, Obhrai C, Peregrine DH, Bredmose H (2007) Violent breaking wave impacts. Part 1: Results from large scale regular wave tests on vertical and sloping walls. Coast Eng 54(8):602–617
5. Bredmose H, Peregrine DH, Bullock GN (2009) Violent breaking wave impacts. Part 2: Modelling the effect of air. J Fluid Mech vol 641
6. Cooker MJ, Peregrine DH (1991) Violent motion as near-breaking waves meet a vertical wall. In: Banner ML, Grimshaw RHJ (eds) Breaking waves. IUTAM symposium, Sydney, 1990, pp 291–297
7. Cooker MJ, Peregrine DH (1992) Wave impact pressure and its effect upon bodies lying on the sea bed. Coast Eng 18(3–4):205–229
8. Peregrine DH (2003) Water wave impact on walls. Ann Rev Fluid Mech 35:23–43
9. Chan ES, Melville WK (1988) Deep-water plunging wave pressures on a vertical plane wall. Proc R Soc Lond A 417:95–131
10. Hull P, Müller G (2002) An investigation of breaker heights, shapes and pressures. Ocean Eng 29:59–79
11. Lugni C, Brocchini M, Faltinsen OM (2006) Wave loads: the role of flip-through. Phys Fluids 18, 122101
12. Colicchio G, Colagrossi A, Lugni C, Brocchini M, Faltinsen O (2007) Challenges on the numerical investigation of the flip-through. In: Proceedings of the 9th International Conference on Numerical Ship Hydrodynamics, pp 380–394
13. Khayyer A, Gotoh H (2009) Modified moving particle semi-implicit methods for the prediction of 2D wave impact pressure. Coast Eng 56:419–440
14. Hunt A (2003) Extreme waves, overtopping and flooding at sea defences. Ph.D. thesis, Department of Engineering Science, University of Oxford
15. Katsardi V, Swan C (2004) The evolution of large waves in shallow water. In: Proceedings of the 29th International Conference on Coastal Engineering, pp 69–81
16. Hasselmann K, Barnett TP, Bouws E, Carlson H, Cartwright DE, Enke K, Ewing JA, Gienapp H, Hasselmann DE, Kruseman P, Meerburg A, Müller P, Olbers DJ, Richter K, Sell W, Walden H (1973) Measurements of wind-wave growth and swell decay during the Joint North Sea Wave Project (JONSWAP). Ergänzungsheft zur Deutchen Hydrographischen Zeitschrift A(8°)(12). 95 pages.
17. Goda Y, Suzuki Y (1976) Estimation of incident and reflected waves in random wave experiments. In: Proceedings of the 15th International Conference on Coastal Engineering, pp 828–845
18. Mansard EP, Funke ER (1980) The measurement of incident and reflected spectra using a least squares method. In: Proceedings of the 17th International Conference on Coastal Engineering, pp 154–172
19. Dean RG, Dalrymple RA (1991) Water Wave Mechanics for Engineers and Scientists. World Scientific, Philadelphia
20. Dold JW, Peregrine DH (1986) An efficient boundary-integral method for steep unsteady water waves. In: Morton KW, Baines MJ (eds) Numerical Methods for Fluid Dynamics II. Oxford University Press, Oxford, pp 671–679
21. Dold JW (1992) An efficient surface integral algorithm applied to unsteady gravity waves. J Comput Phys 103:90–115
22. Tanaka M, Dold JW, Lewy M, Peregrine DH (1987) Instability and breaking of a solitary wave. J Fluid Mech 135:235–248
23. Cooker MJ, Vidal C, Dold JW, Peregrine DH (1990) The interaction between a solitary wave and a submerged semicircular cylinder. J Fluid Mech 215:1–22
24. Cooker MJ (1990) The interaction between steep water waves and coastal structures. Ph.D. thesis, School of Mathematics, University of Bristol, UK
25. Trefethen L (1980) Numerical computation of the Schwarz-Christoffel transformation. SIAM J Sci Stat Comput 1:82–102
26. Schäffer HA, Steenberg CM (2003) Second-order wavemaker theory for multidirectional waves. Ocean Eng 30:1203–1231
27. Hunt A, Taylor P, Borthwick A, Stansby P, Feng T (2004) Phase inversion and the identification of harmonic structure in Coastal Engineering experiments. In: Proceedings of the 29th International Conference on Coastal Engineering, Lisbon, pp 1047–1059
28. Peregrine DH, Bredmose H, Bullock GN, Obhrai C, Müller G, Wolters G (2004) Water wave impact on walls and the role of air. In: Proceedings of the 29th International Conference on Coastal Engineering, Lisbon, pp 4005–4017
29. Madsen PA, Bingham HB, Schäffer HA (2003) Boussinesq-type formulations for fully nonlinear and extremely dispersive water waves: Derivation and analysis. Proc R Soc Lond A 459(2033):1075–1104